Non-uniform Temperature Distribution's Impact on Downhole Weight on Bit Measurement (DWOB) and the Novel Compensatory Method

Chao Wang, China University of Petroleum, Beijing; Gonghui Liu , China University of Petroleum, Beijing; Jun Li, China University of Petroleum, Beijing; Tao Zhang, Beijing Information Science and Technology University; Zhirong Yang, Norwegian University of Science and Technology; Hailong Jiang, Beijing Information Science and Technology University; Kai Ren, China University of Petroleum, Beijing; Zhe Wu, China University of Petroleum, Beijing

Abstract

Non-uniform temperature distribution of DWOB measuring devices has a great effect on the accuracies of weight on bit (WOB) readings. To study the influence, two types of non-uniform temperature distributions of the WOB measuring device were created. The relationship between the two temperature distributions was studied with the further transform of heat conduction formulas. Then the strain of the measuring device was acquired under the two temperature distributions. And the relations of the strain in the two conditions was obtained with the further transform of compatibility equations and constitutive equations. To quantify the influence of non-uniform temperature distribution, a contrast simulation without non-uniform temperature distribution was carried out. The simulated results showed that the WOB errors were 9.33 kN and 46.25 kN. This paper proposed a novel compensating method based on the deduced relationships above, with which the WOB error was eliminated to 0.4kN. To further validate the new method, the laboratory heating and cooling experiments were carried out. The experiment showed that the biggest WOB error was eliminated to 1.7 kN while the original error was up to 60 kN. Then a field experiment was conducted. Eight connection processes are chosen to further elaborate the temperature difference's impact and the related compensatory method. The economic loss caused by the WOB measuring inaccuracy was calculated, which was up to 1.17% of the drilling cost per meter. The work presented herein can serve as guidance for the DWOB measurement.

Keywords

DWOB measurement
Non-uniform temperature distribution
Heating and cooling experiments
Field experiment
Novel compensatory method

1. Introduction

Rate of penetration (ROP) is an important parameter to evaluate the drilling process and it is greatly influenced by WOB. The optimized WOB can produce high ROP, which helps to reduce the drilling time(Irawan et al., 2012). Excessive WOB will cause drill string buckling, excessive stick-slip vibration, and exceeding downhole equipment design loads (Zha et al., 2018). It is necessary to obtain accurate WOB before optimizing it. The most common way to acquire it is using the difference between the hookload and the floating weight of drill strings(Saputelli et al., 2003).

This method is called ‘Surface measurement’. Unfortunately, surface measurement is not reliable especially in the drilling process of high angle deviated wells and horizontal wells (Boucher et al., 2005). The main reason is that the drag force between the well walls and the drill strings is hard to predict. Imperfect weight transfer causes estimates based on surface data to be much higher than downhole measurements(Pink et al., 2012). Analytical or finite element models can provide better estimates for DWOB(Wu and Hareland, 2012). There are some attempts to correct the surface measurement method by combining well trajectory and analytical models (Hareland et al., 2014; Mason and Chen, 2007). To acquire more accurate DWOB, drilling engineers turned to ‘Downhole Measurement’. From the 1970s, more and more near-bit WOB measuring devices have been invented. These devices were equipped with strain gauges, forming Wheatstone Bridges. And the measured data was transferred to the surface via MWD in real time (Das and Song, 1995; Pink et al., 2013; Roberts et al., 2005; Wassell, 2003). This direct method has improved the accuracy to a great extent. Nevertheless, the WOB measuring devices are subjected to significant inaccuracies due to the temperature variations and the non-uniform temperature distribution (Blanchette and Getzlaf, 2015).

The resistance of the strain gauges fixed on the WOB measuring devices will change linearly with the change of WOB. Considering that the resistance of the strain gauges is not only dependent on the strain but also dependent on the temperature(Grosso et al., 1983), the change in temperature can lead to inaccuracies in the WOB measurement (Hutchinson, 2014). The downhole temperature grows higher when the well depth grows deeper. To compensate for the thermal strains induced by temperature variations, Wheatstone bridges are typically employed (Das and Song, 1995; Tanguy and Leising, 1982). This method has achieved significant improvements in the accuracy of down-hole WOB measurement.

However, there are some non-ignorable errors originating from non-uniform temperature distribution. The annulus temperature and the temperature of the fluid within the drill string are typically different, with the annulus temperature being slightly higher (Wassell et al., 2013). And it leads to the existence of the temperature difference inside the measuring devices, which is shown in **Fig. 1**.

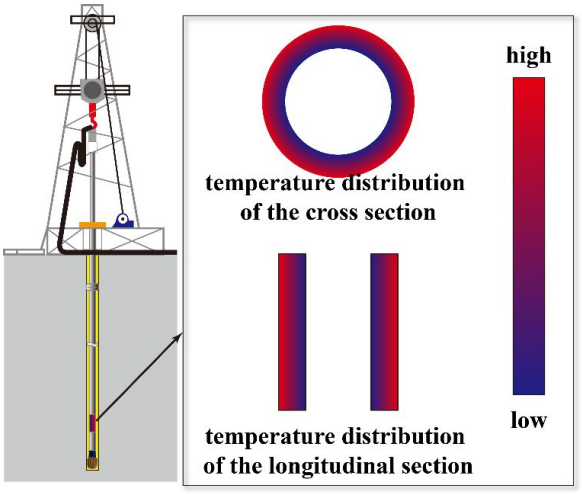

Fig.1—Temperature distribution inside the measuring devices

When non-uniform temperature distribution occurs, the expansion and contraction of some parts are restrained because of the influence of adjacent parts with different temperatures. Then the additional stress comes into being. The strain gauges will sense the additional strain, leading to extra WOB readings. Today there are few related types of research about how to eliminate the extra WOB readings. To solve the similar problem occurred in the thermal stress determination of thick-wall boiler components, boiler manufacturers determine the thermal stresses based on the temperature measurement in the middle of the wall thickness and near the inner surface of the element (Taler et

al., 2018; Taler et al., 2016). Namely, the temperature distribution is deduced by treating some measured points as boundary conditions. And then the thermal stress is calculated subsequently with thermodynamic formulas. Similarly, temperature sensors are added into the drill collar to further permit non-uniform temperature distribution compensation (Wachtler and Yang, 1986; Wassell, 2003; Woloson and Jones, 2001). These temperature sensors are used for a steady state temperature correction. But the mechanism and the concrete compensating method are not been elaborated. A taring procedure, determining the zero-WOB, was carried out during a connection to eliminate the drifts induced by temperature (Sutcliffe and Sim, 1991). More advanced, an automated zero-WOB detection was proposed based on low variance, clustering, SAX algorithm and so on(Baumgartner et al., 2019). The two taring methods are easy and effective to be carried out if the temperature difference between the inner and annular remains unchanged. While the temperature difference is closely related to the pump rate, which is not a constant. A new temperature compensatory method based on biaxial superimposed strain gauges performed well (Wang et al., 2018). However, this method needs more strain gauges and the stability will become worse.

Previous compensatory methods (Baumgartner et al., 2019; Das and Song, 1995; Grosso et al., 1983; Hareland et al., 2014; Sutcliffe and Sim, 1991; Tanguy and Leising, 1982; Wachtler and Yang, 1986; Wang et al., 2018; Wassell, 2003; Woloson and Jones, 2001) have made significant contributions to WOB measurement. However, the impact of temperature difference between the inside wall and outside wall of the measuring device could still not be eliminated perfectly. To further improve the measurement accuracies, the following researches have been carried out in this research paper: (1) The temperature distribution of the measuring device when drilling; (2) The detailed strain of each measuring point under the non-uniform temperature distribution and other outer force; (3) The measured WOB error acquired based on the Wheatstone bridge; (4) A novel WOB correcting method aiming to eliminating the effect of non-uniform temperature distribution.

To validate the new method, a laboratory experiment was conducted. The experiment consisted of two heating stages and seven cooling stages. The heating stages could make sure that the outer wall's temperature was higher than the inner wall. And the cooling stages are used to create a phenomenon, where the outer wall's temperature was lower than the inner wall. To further validate the new method, a field experiment was carried out. Eight connection processes are chosen to elaborate the temperature difference's impact and the related compensatory method. At the end of the article, we evaluated the economic loss caused by the WOB measuring inaccuracy to emphasize the practical value of this work(Jia et al., 2019).

The proposed method may be used for achieving improved WOB measurement, and can be significant in improving bit life and ROP.

2. Impact of non-uniform temperature distribution on WOB measurement

2.1 Strain gauges' strain while drilling

The formation's temperature is higher than fluid's temperature with the same well depth (Shi et al., 2018; Shi et al., 2019a; Song et al., 2017; Yao et al., 2018; Zhang et al., 2018). Heat exchange among formation, annulus drilling fluid, drilling devices and inner drilling fluid occurs when drilling. According to the heat transfer direction, the annulus drilling fluid temperature is higher than the inner drilling fluid temperature. Thus the outer wall's temperature of measuring device is higher than the inner wall's temperature.

Many scholars have studied the heat transfer of geothermal systems during drilling operations,

using both analytical and numerical methods to estimate the circulating fluid temperature (Al Saedi et al., 2018; Holmes and Swift, 1970; Li et al., 2015; Ramey, 1962; Shi et al., 2019b). The typical temperature profile inside the drilling devices and annulus temperature profile with the well depth is shown as **Fig. 2** (Kabir et al., 1996).

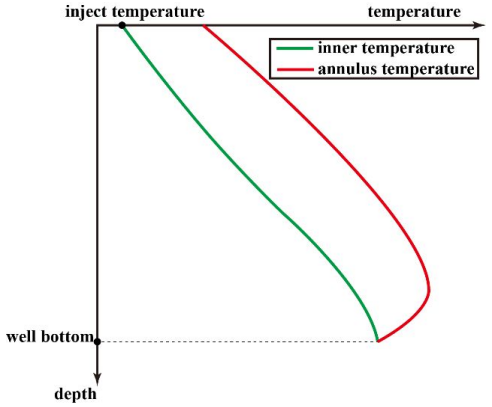

Fig.2—Typical temperature profile inside the drilling devices and annulus pressure profile

The measuring device is usually installed near the bit. The shorter the distance between the measuring device and bit is, the less temperature difference between the inner drilling fluid and the annulus drilling fluid is according to Fig.2. The quantification of temperature difference between the inside wall and the outside wall is discussed in **Appendix A**.

The distance between the measuring device and bit is usually from 10 m to 50 m. Here we suppose the temperature difference between the inner drilling fluid and the annulus drilling fluid is 0.8 ℃ to 4 ℃.

To study temperature's influence on the strain of each strain gauge used to measuring DWOB, three groups of finite element numerical simulation were carried out.

2.1.1 Model description

2.1.1.1 Physical model

The three-dimensional model used for simulation and the real object are shown as **Fig.3**. The positions where the strain gauges are installed can be found in Fig.3 (b) and Fig.3 (c). The geometry model contains two parts, the cavity part and the solid part. The cavity is used for holding single computing chips and wires. The solid part is made of non-magnetic structural steel and there is a cylindrical hollow run through the solid part used for fluid passage. The density, Young's model and Poisson's ratios of the solid part are 7850 kg/m^3, 210 GPa and 0.3 respectively. Other structural parameters are shown in Fig.3.

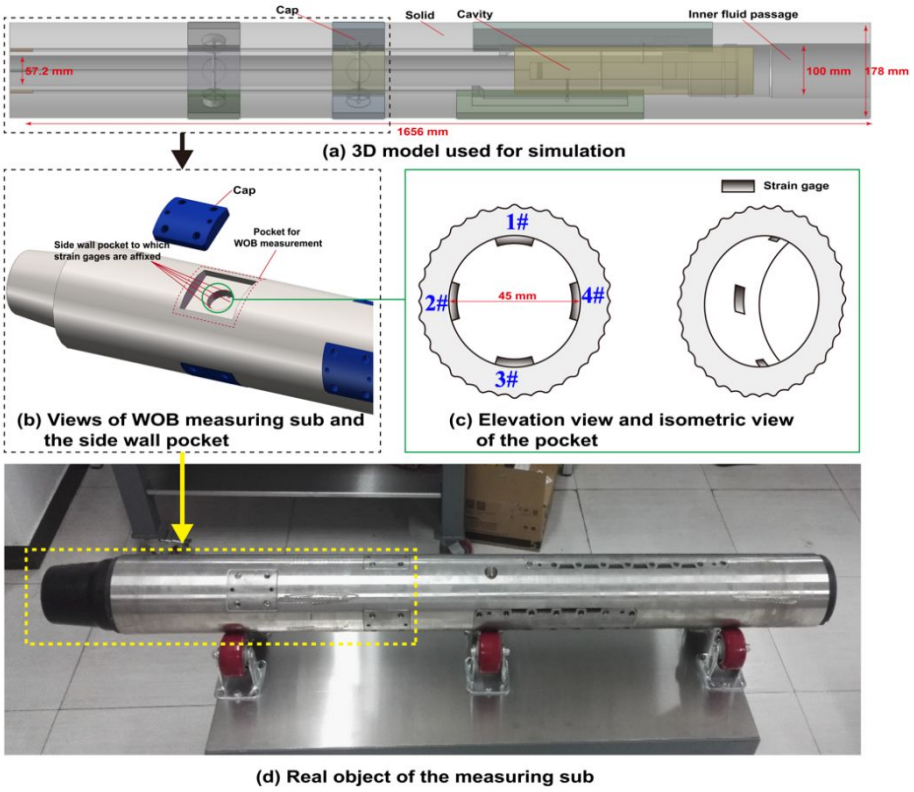

Fig.3—3D simulating model and the real object

The process of how to convert the physical model to the simulation model is described in **Appendix B.**

The simulated conditions of the three groups of finite element numerical simulation are shown in **Table.1**.

Table. 1—Parameters of three groups of simulation

Group number	Inner wall temperature (℃)	Outer wall temperature (℃)	Outer force acted on two ends (kN)
1	-	-	30.0
2	140.0	140.8	0.0
3	140.0	144.0	0.0

2.1.1.2 Thermal transfer model

The main type of heat transfer in the solid part is heat conductivity, which is controlled by the Fourier law. It can be defined as

$$\boldsymbol{q} = -\kappa \nabla T \tag{1}$$

The partial differential equation of heat conduction in the WOB measuring tool is

$$\mathrm{div}\left(\kappa \nabla T\right) + W - c\rho_s \frac{\partial T}{\partial t} = 0 \tag{2}$$

Because there is no heat source inside the measuring device (W=0) and the thermal conductive mediums are isotropic, the heat conduction differential equation of the measuring device in a generalized coordinate system can be expressed as (Saeid et al., 2013; Xu et al., 2015)

$$\frac{\partial T}{\partial t} = a\nabla^2 T \tag{3}$$

2.1.1.3 Thermal-elastic model

The geometric equations of thermo-elastic materials can be expressed as

$$\varepsilon_i = \frac{\partial u_i}{\partial x_i}, \gamma_{ij} = \frac{\partial u_i}{\partial x_j} + \frac{\partial u_j}{\partial x_i} \tag{4}$$

Constitutive equations can be written as

$$\boldsymbol{E} = \frac{1}{E}\left[(1+\mu)\boldsymbol{T} - \mu\Theta\boldsymbol{I}\right] + \alpha\Delta T\boldsymbol{I} \tag{5}$$

Where $\Theta=\sigma_{ii}$ and $\boldsymbol{I}=\delta_{ij}$. The equilibrium equation is

$$div\boldsymbol{T} + \rho\boldsymbol{b} = \rho\boldsymbol{a} \tag{6}$$

Where $\rho\boldsymbol{b}$ stands for body force and $\boldsymbol{a}$ is the acceleration. In this work, the item $\rho\boldsymbol{a}$ can be neglected when compared with axial force. Then the indexes form of Eq.6 can be expressed as

$$T_{ji,j} + \rho b_i = 0 \tag{7}$$

Eq.7 can be further written as

$$\overline{T}_{ji,j} = 0, \text{ where } \begin{cases} \overline{T}_{ji,j} = T_{ji,j}, i \neq j \\ \overline{T}_{ii,i} = T_{ii,i} + \rho b_i \end{cases} \tag{8}$$

Then the equilibrium equations turns into homogeneous equations, which helps to conduct analysis.

The compatibility equations are also needed to conduct the solving process, and they can be expressed as

$$\nabla^2\boldsymbol{T} + \frac{1}{1+\mu}\nabla\nabla\Theta = -\alpha E\left(\frac{1}{1-\mu}\nabla^2 T + \frac{1}{1+\mu}\nabla\nabla T\right) \tag{9}$$

2.1.1.4 Simulation mesh

The temperature solver FLUNT and the finite element solver ANSYAS Workbench were used to solve the partial differential equations of mathematical model. The example of the mesh schemes for the WOB measuring tool is shown in Fig.4.

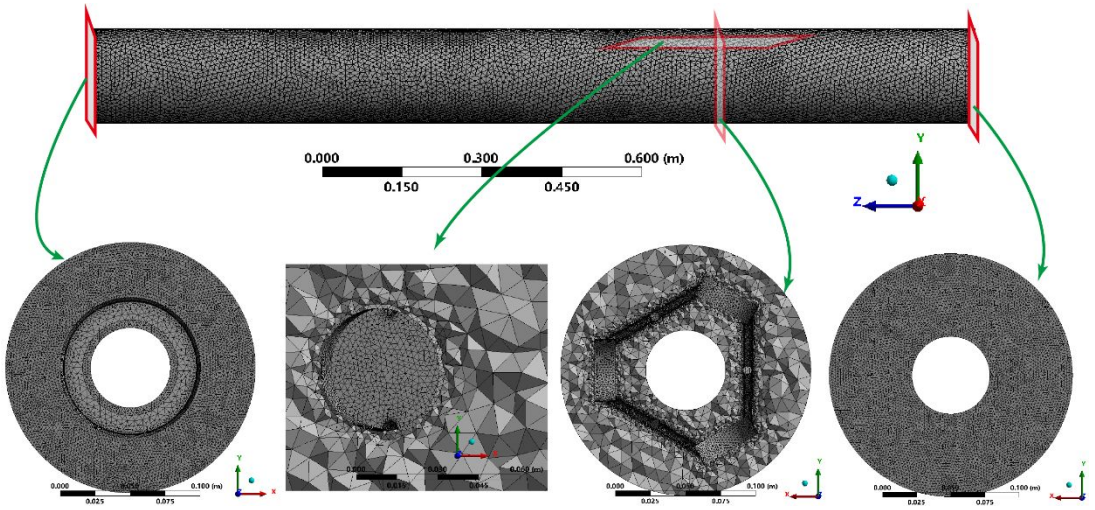

Fig.4—Numerical meshing schemes

Tetrahedral meshing scheme method is employed because of the inner complex structure. The places, where the strain gauges are pasted, adopt local grid refinement method to acquire more accurate result. The meshes near the end faces are refined to reduce the boundary effects. The refined meshes share the same meshing scheme method. The mesh number and size of the rest place are the

parameters to be optimized.

To make sure that the simulated results are independent of the mesh number, the temperature and the strain of the 1# strain gauge in group 3 simulation with different mesh numbers are shown in Fig.5.

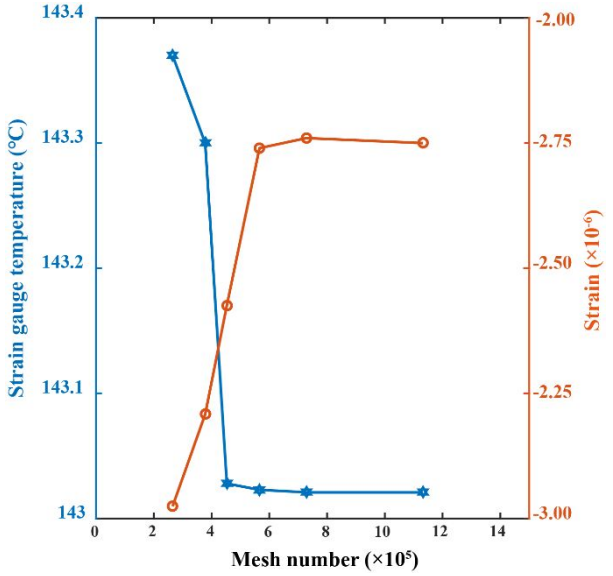

Fig.5—Temperature and strain of 1# strain gauge under various mesh numbers

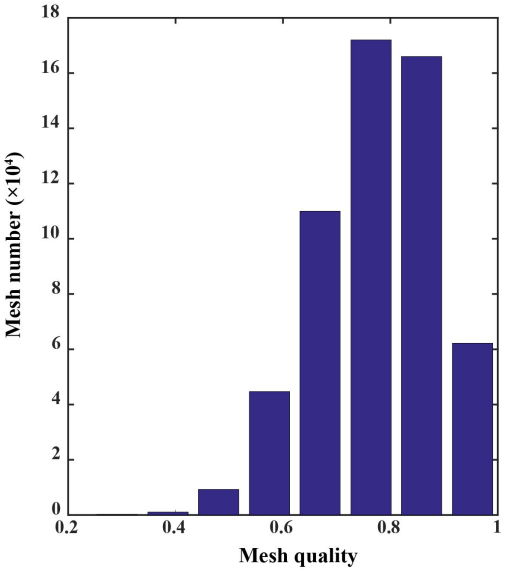

Fig.6—Mesh quality distribution when the whole mesh number is 565966

From Fig.5, the strain gauge temperature decreased with the mesh number and the temperature tended to be constant when the mesh number exceeded 476324. As to the strain, it increased with the growth of mesh number and remained stable after the mesh number reached 565966. Hence, the whole mesh number was determined to be 565966 for the simulation precision. Fig.6 shows the mesh quality distribution when the whole mesh number is 565966. The average mesh quality is 0.77336, which guaranteed the accuracy of the results further.

2.1.2 Temperature distribution and strain analysis

2.1.2.1 Temperature distribution analysis

The numerical simulations of temperature distribution are based on Fluent, and the strain simulations are carried out using Static Structural model. During the simulation, the reference body temperature is 22 ℃.

The temperature distribution of Group **2** and Group **3** experiment is shown in **Fig.7**. It can be obviously found that the temperature distribution is non-uniform and the shorter the distance to the outer wall, the higher the temperature is.

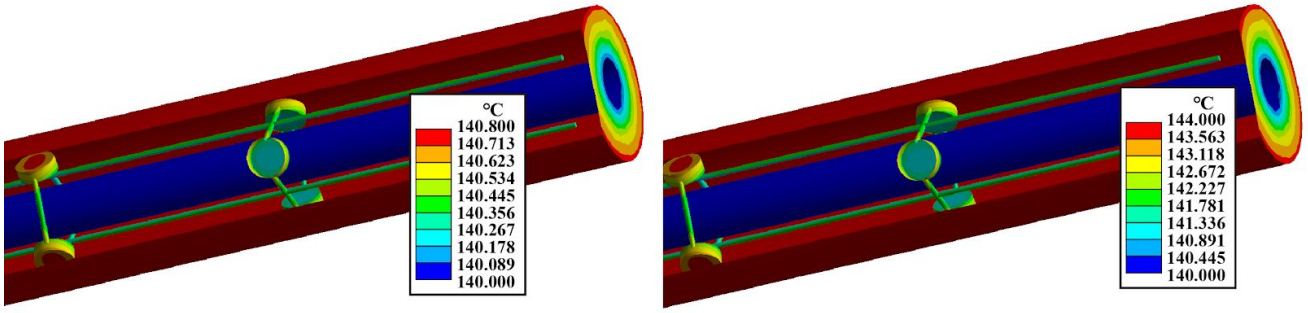

(a) Temperature distribution of Group 2 (b) Temperature distribution of Group 3

Fig.7—Simulated results of temperature distribution

It's interesting that the two contours in Fig.7 are nearly the same. To quantify the relationship of

temperature distribution in Group 2 and Group 3, the value each color representing in the two contours is shown in **Fig.8**.

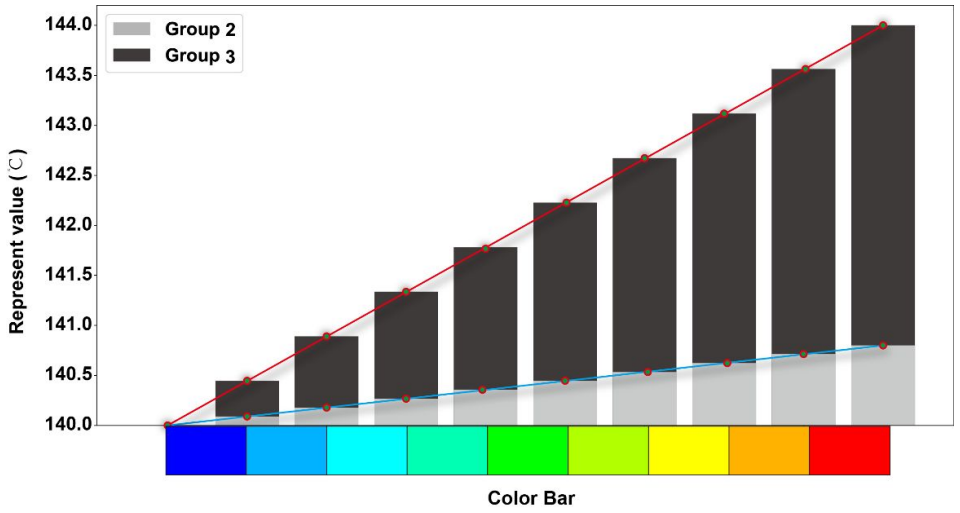

Fig.8—Color bar value in two groups simulation

The above red line's gradient is five times of the lower line's gradient, which equals to the temperature difference of inner wall and outer wall in Group 3 divided by the temperature difference in Group 2. This can be explained as follows.

When the temperature distribution stays steady, Eq.3 can be written as

$$a\nabla^2 T=0 \tag{10}$$

The heat conduction process can be approximately regarded as a steady heat conduction process when drilling. Then the conduction differential equation 10 can be further expressed as

$$\nabla^2\left(k\left(T-T_{innerWall}\right)\right)=0 \tag{11}$$

An interesting conclusion can be deduced from Eq. 11. Assume the temperature of the inner wall, any inner point, and the outer wall are $T_{\text{innerWall0}}$, T_{inner0} and $T_{\text{outerWall0}}$ at one moment. And at another moment these temperatures become $T_{\text{innerWall1}}$, T_{inner1} and $T_{\text{outerWall1}}$. Then the following relationship can be made.

$$\frac{T_{inner1}-T_{innerWall1}}{T_{inner0}-T_{innerWall0}}=\frac{T_{outerWall1}-T_{innerWall1}}{T_{outerWall0}-T_{innerWall0}} \tag{12}$$

2.1.2.2 Strain analysis

It should be noted that the calculated thermal strain is $\alpha\Delta T$, not including the strain due to non-uniform temperature distribution. Here the cylindrical coordinate system is adopted considering the shape of the circle pocket to hold strain gauges.

To explore the influence of non-uniform temperature distribution, a contrast simulated Group 1 experiment was carried out and every part's temperature was the same. In the Group 1 simulation, one end of the measuring device is fixed and the other end is pressurized with 30000 N. The simulated result is shown as **Fig. 9**.

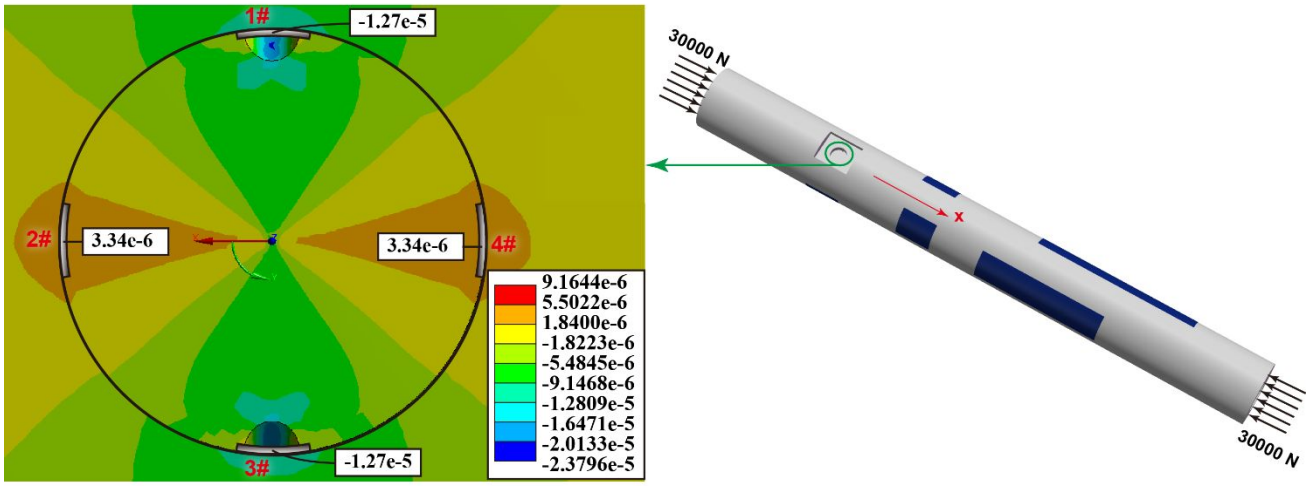

Fig. 9—Circumferential strain under external force 30 kN

The strain gauges 1# and 3# are in the compression status while strain gauges 2# and 4# are in tension seen from the simulated results in Fig.9. What's more, the absolute value of compression strain is much larger than that of tension strain due to the ratio of the device's length to its width being so large. If the outer pressure force turns to *k* times of the original value, the difference between the strain of 1# and 4# will also go to *k* times of its original value due to the stress and strain superposition principle.

To further quantify the impact of non-uniform temperature distribution, two different kinds of temperature distribution act on the measuring device without any external force. The simulated results of group 2 and group 3 are shown in **Fig.10** and **Fig.11** respectively. When the temperature of two adjacent parts is different, the expansion or contraction is different leading to the mutual constraint. Thermal stress is originated from this mutual constraint. The extra strain generates at the same time, which equals the circumferential strain in Fig.10 and Fig.11. Here the circumferential strain is the whole strain minus thermal strain ($\alpha\Delta T$).

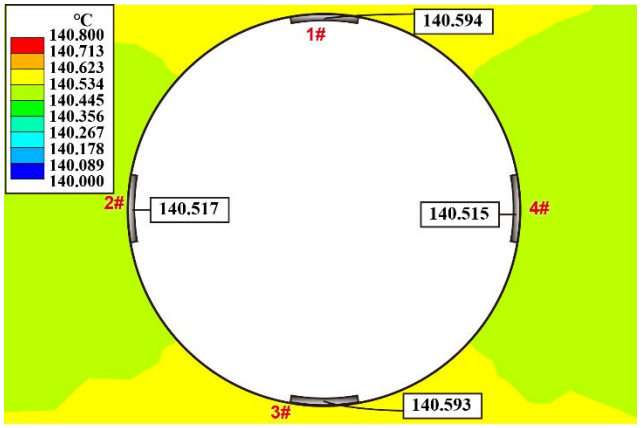

Fig.10 a—Temperature distribution of the 4 strain gauges in Group 2

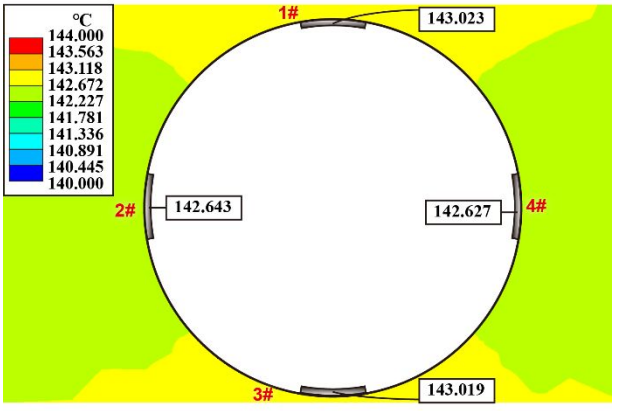

Fig.11 a—Temperature distribution of the 4 strain gauges in Group 3

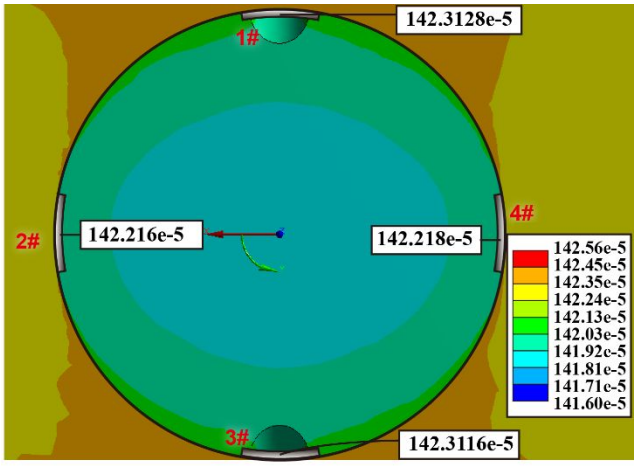

Fig.10 b—thermal strain of the 4 strain gauges in Group 2

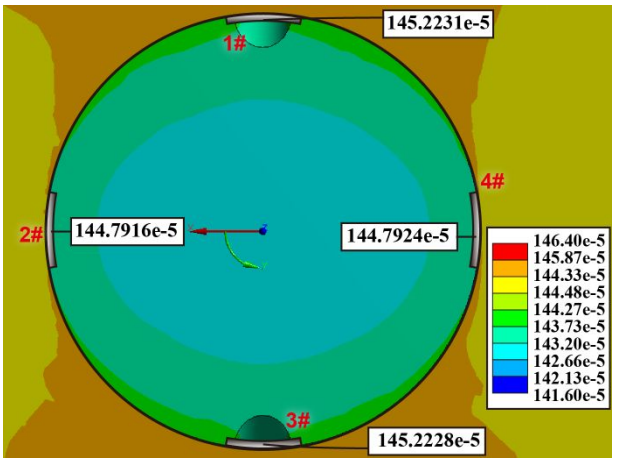

Fig.11 b—thermal strain of the 4 strain gauges in Group 3

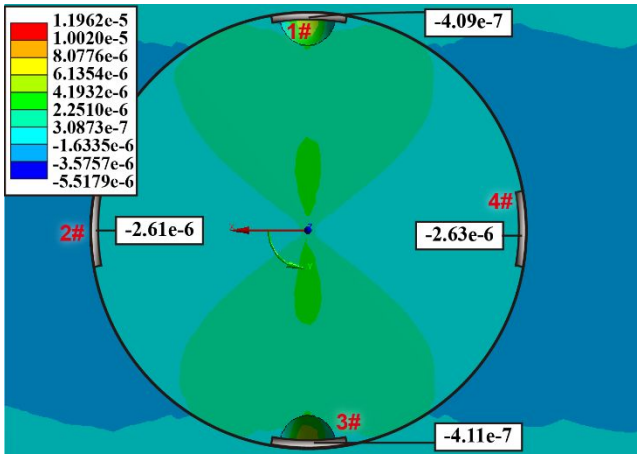

Fig.10 c—Circumferential strain of the 4 strain gauges due to non-uniform temperature distribution in Group 2

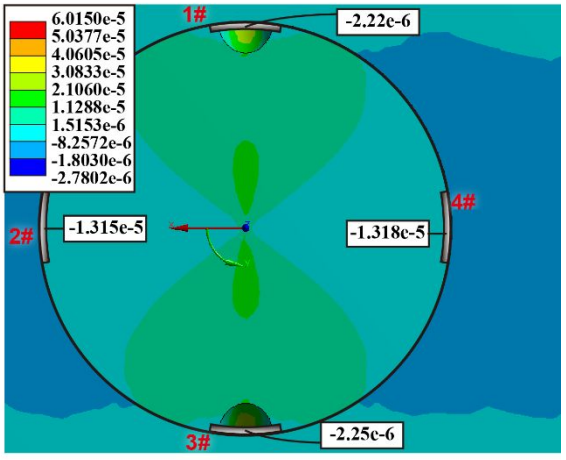

Fig.11 c—Circumferential strain of the 4 strain gauges due to non-uniform temperature distribution in Group 3

Due to the special structure of the measuring device and the temperature difference of the inner wall and the outer wall, the temperature of the 4 strain gauges is differently shown in Fig.10 a and Fig.11 a. The thermal strain of the 4 strain gauges is also different, with the strain of 1# and 3# larger than that of 2# and 4#. While the circumferential strain of the 4 strain gauges is a compressive strain, with the absolute strain value of 1# and 3# smaller than that of 2# and 4#. What's more, the circumferential strain in Fig.11 c is nearly 4 times the strain in Fig.10 c. The reason is as follows.

When coupling the inner wall's temperature into Eq.9, the stress compatibility equations due to no-uniformed temperature distribution can be further expressed as

$$\nabla^2 \boldsymbol{T} + \frac{1}{1+\mu}\nabla\nabla\Theta = -\alpha E\left[\frac{1}{1-\mu}\nabla^2\left(T - T_{innerWall}\right) + \frac{1}{1+\mu}\nabla\nabla\left(T - T_{innerWall}\right)\right] \tag{13}$$

If the temperature increases to k times as much as it used to be, the following equation can be made.

$$\nabla^2\left(k\boldsymbol{T}\right) + \frac{1}{1+\mu}\nabla\nabla\left(k\Theta\right) = -\alpha E\left\{\frac{1}{1-\mu}\nabla^2\left[k\left(T - T_{innerWall}\right)\right] + \frac{1}{1+\mu}\nabla\nabla\left[k\left(T - T_{innerWall}\right)\right]\right\} \tag{14}$$

Considering the circumferential strain is originated from the thermal stress, then the relationship between circumferential strain and the thermal stress can be expressed as

$$(k\boldsymbol{E}) = \frac{1}{E}\left[(1+\mu)(k\boldsymbol{T}) - \mu\Theta(k\boldsymbol{I})\right] \tag{15}$$

It's interesting that the thermal strain difference of gauge 1# and 4# in is Fig.11 b almost 4 times as much as that in Fig.10 b, which can be explained by the further transform of Eq.12.

$$\frac{\alpha\left(T_{inner1} - T_{innerWall1}\right)}{\alpha\left(T_{inner0} - T_{innerWall0}\right)} = \frac{T_{outerWall1} - T_{innerWall1}}{T_{outerWall0} - T_{innerWall0}} \tag{16}$$

We use the difference between the strain of 1# and 4# to measure the axial force. However, the difference is zero even when there is no axial force from the above analysis.

2.2 Methods to compensate thermal strain and circumferential strain

The typical and effective method to compensate for temperature difference is electrically coupling the strain gauges to form a Wheatstone bridge. In the prior works (Tanguy and Leising, 1982; Wassell, 2003), uniaxial strain gauges were coupled to form the Wheatstone bridge, as shown in **Fig. 12**.

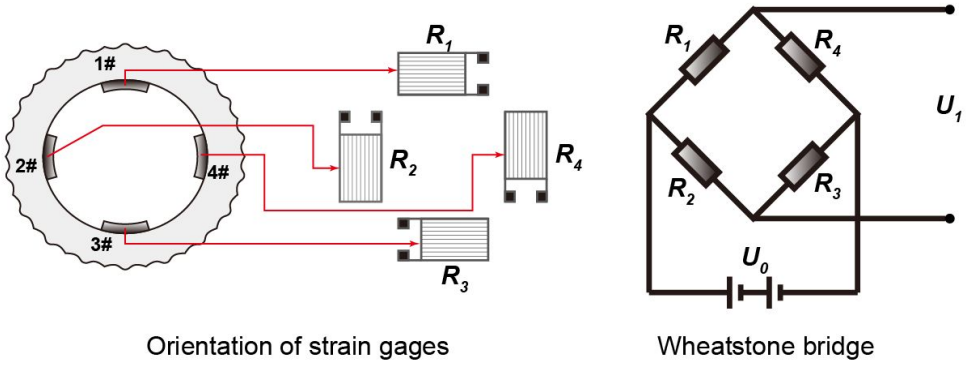

Fig.12—Uniaxial strain gauges form Wheatstone bridge

The voltage output of this kind of Wheatstone bridge in Fig.12 can be expressed as (Wang et al., 2018)

$$U_1 = \frac{U_0}{4}\left\{\left[\alpha_R + K\left(\alpha_s - \alpha_g\right)\right]\sum_{i=1}^{4}(-1)^{i+1}\Delta T_{si} + K\sum_{i=1}^{4}(-1)^{i+1}\Delta\varepsilon_{\sigma i}\right\} \tag{17}$$

From Eq. 17, it can be deduced that the strain errors caused by the change in temperature can be apparently completely removed if the position of each strain gauge pasted on the substrate surface is the same. And this part strain is called apparent strain. According to the analysis of section 2.1.1 and 2.1.2, the change of normal strain $\Delta\varepsilon_{\sigma i}$ consists of three parts axial force, thermal strain and circumferential strain due to the mutual constraint.

The apparent strain of the used strain gage is the function of temperature and the relationship is shown in **Fig. 13**.

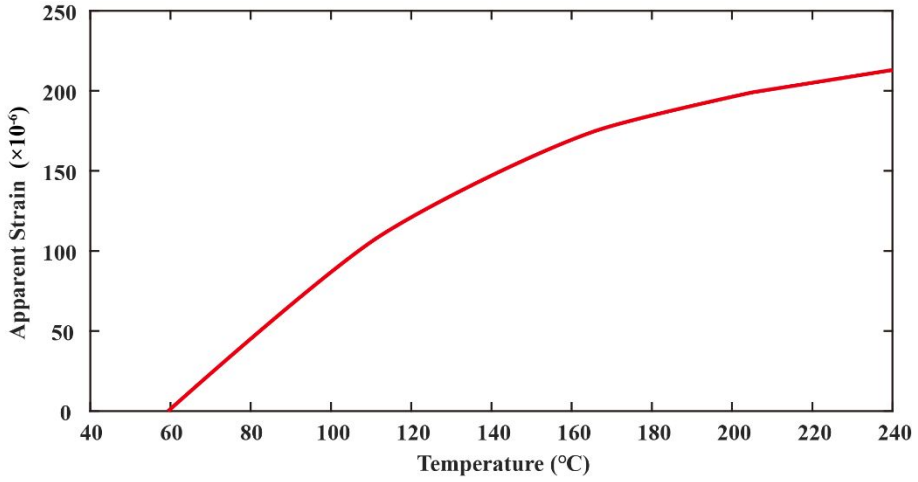

Fig.13—Apparent strain varying with temperature

The term $[\alpha_R+K(\alpha_S-\alpha_g)]$ is the gradient of the apparent strain varying with temperature. $[\alpha_R+K(\alpha_S-\alpha_g)]$ is 1.22×10^{-6}/℃ when the temperature is close to 140 ℃.

Then the value of the items inside the curly braces of Eq. 17, true WOB and apparent WOB in the 3 groups of simulated experiments are shown in **Table. 2**.

Table. 2—Output of Wheatstone Bridge

Temperature difference ℃	$\left[\alpha_R+K\left(\alpha_s-\alpha_g\right)\right]\sum_{i=1}^{4}(-1)^{i+1}\Delta T_{si}$	$K\sum_{i=1}^{4}(-1)^{i+1}\Delta\varepsilon_{\sigma i}$	$\left[\alpha_R+K\left(\alpha_s-\alpha_g\right)\right]\sum_{i=1}^{4}(-1)^{i+1}\Delta T_{si}$ $+K\sum_{i=1}^{4}(-1)^{i+1}\Delta\varepsilon_{\sigma i}$	True WOB (kN)	Apparent WOB (kN)
0	0	-3.01×10^{-5}	-3.01×10^{-5}	30	30
0.8	9.39×10^{-8}	9.26×10^{-6}	9.36×10^{-6}	0	-9.33
4	4.63×10^{-7}	4.59×10^{-5}	4.64×10^{-5}	0	-46.25

It can be illustrated that the part of apparent WOB due to temperature difference among the strain gages is very little seen from the results of group 2 and 3. This is to say the strain errors caused by the change in temperature can be ultimately removed, although the temperature of each gauge cannot be the same because of the structure of the measuring apparatus. However, the non-uniform distribution of temperature makes a great contribution to the whole apparent WOB. $K\sum_{i=1}^{4}(-1)^{i+1}\Delta\varepsilon_{\sigma i}$ is almost 100 times as much as $\left[\alpha_R+K\left(\alpha_s-\alpha_g\right)\right]\sum_{i=1}^{4}(-1)^{i+1}\Delta T_{si}$. Namely, the impact of non-uniform distribution of temperature could not be completely eliminated with this method.

According to Eq.14 to Eq.16, the following conclusion can be made. When $(T - T_{\text{innerWall}})$ becomes k times as much as it used to be, the stress σ due to non-uniform temperature distribution would become k times as much as they used to be. Then the normal strain ε due to non-uniform temperature distribution would also become k times as much as they used to be. The part Wheatstone bridge output $K\sum_{i=1}^{4}(-1)^{i+1}\Delta\varepsilon_{\sigma i}$ due to non-uniform temperature distribution would become k times as much as they used to be at the same time.

With this conclusion, we can propose the method to compensate the strain due to the non-uniform distribution of temperature. Firstly, at one moment, we acquire the apparent WOB (WOB_{a0}), the temperature difference (ΔT_0) between the inner fluid's temperature and the annulus fluid's temperature when the drilling fluid is in circulation and the true WOB is zero. At another moment, the two parameters become WOB_{a1} and ΔT_1. Then the true WOB can be expressed as

$$WOB = WOB_{a1} - \frac{\Delta T_1}{\Delta T_0} WOB_{a0} \tag{18}$$

Take the simulated results of group 2 and group 3 as an example to depict the new method. The real WOB is zero when conducting group 2 experiment, and ΔT_0=0.8 ℃, WOB_{a0}=-9.33 kN. The apparent WOB (WOB_{a1}) is -46.25 kN and the temperature difference (ΔT_1) is 4 ℃ when conducting group 3 experiment. Now use Eq.18 to deduce the real WOB during group 3 experiment. It is $-46.25 - \frac{4}{0.8}(-9.33) = 0.4$ kN, which is close to the real value 0. The error is originated from mesh quality when doing finite element calculation.

3. Validation via laboratory heating and cooling experiments

The purpose of the experiment is to study the influence of the non-uniform distribution of temperature in the measuring device to the WOB measurement when there is no external loads. The designed experimental apparatus is primarily constituted with the WOB measuring apparatus, power supply, water container, heating wire and temperature controller, as shown in **Fig. 14a**. **Fig. 14b** shows the schematic diagram of the experimental devices. The WOB measuring apparatus can measure the annular temperature simultaneously. According to the simulated results, the inner wall's temperature also influences the measurement of WOB. So we use the thermometer to measure the inner wall's temperature. The sampling frequency of WOB and the outer wall's temperature is 100Hz, and the inner wall's temperature is recorded about every 4 minutes.

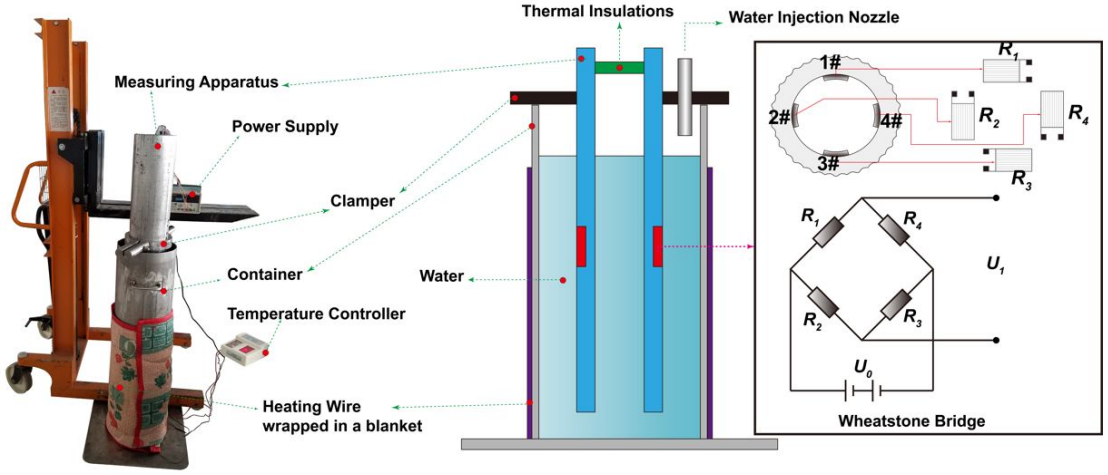

Fig.14—Experimental apparatus

Considering it is difficult to control the temperature of the inner wall and the outside wall, we created the non-uniform distribution of temperature inside the measuring device by heating and cooling from the outside seen in Fig. 14. The experimental process consist of 9 parts.

①. At the beginning, put the measuring device into the hot water and turn on the heating device.

②. At time t_0, put 85 ℃ water into the container from the annular between the out wall of the measuring device and the container.

③. At time t_1, turn off the heating device and pour 8 ℃ cold water into the annular.

④. At time t_2, pour 8 ℃ cold water into the annular.

⑤. At time t_3, pour 8 ℃ cold water into the annular.

⑥. At time t_4, pour 8 ℃ cold water into the annular.

⑦. At time t_5, pour 8 ℃ cold water into the annular.
⑧. At time t_6, pour 8 ℃ cold water into the annular.
⑨. At time t_7, pour 4 ℃ cold water into the annular.

During the experiment, the bottom end of the measuring device did not touch the container. Namely there is no WOB. However, the reading of the WOB measuring sensor is not zero. The result is shown in **Fig.15**.

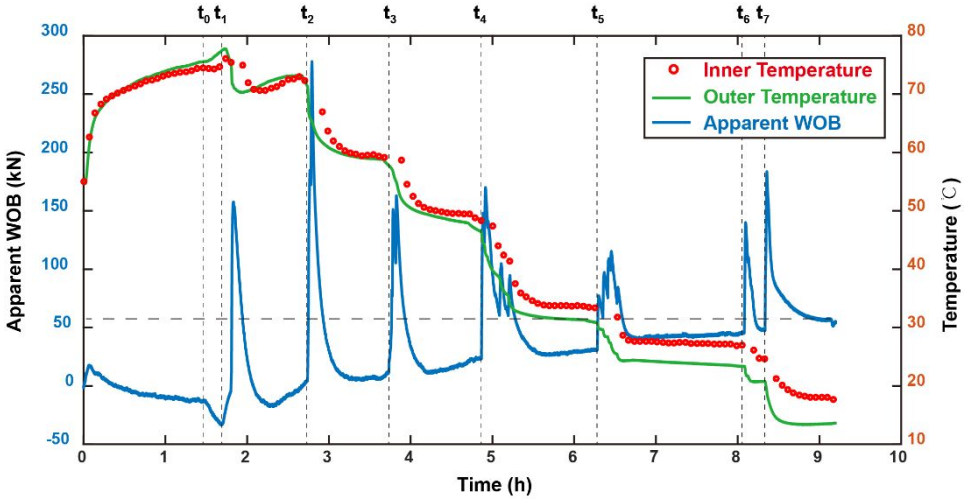

Fig.15—Experimental results

From the beginning to t_0, the measured annulus and inner temperature are increasing while the apparent WOB is decreasing on the whole. When heating, the outer wall's temperature was slightly higher than the inner wall of the measuring device due to the direction of heat conduction. According to the simulated results above, the apparent WOB is negative when the outer wall's temperature is higher than the inner wall's temperature. And this corresponds with the experiment results.

After pouring 85 ℃ hot water into the annular, the difference between the outer and inner wall would increase and the absolute value of WOB would increase at the same time. At the time t_1, the apparent WOB increased rapidly, because 8 ℃ cold water was poured into the container and the temperature of the outer wall is much lower than the inner wall in a short time. Then due to the thermal convection, the temperature difference between the inner wall and outer wall became smaller and the apparent WOB decreased sharply.

After turning off the heating device, the heat conduction direction was from the inner to the outer because the environmental temperature is lower than that of the experimental system. Namely, the inner wall's temperature is higher than the outer wall, and the apparent WOB would project an increasing pulling force, which met the simulated results.

Considering the cold water was pulled into the annular at t_2 to t_7, the temperature of both inner and outer wall decreased and the temperature difference of them increased leading to the increasing of the apparent WOB.

Here we regard the expression $WOB_{apparent}/\left(T_{innerwall}-T_{outerwall}\right)$ as the influenced rate of temperature difference, which is shown in **Fig.16**.

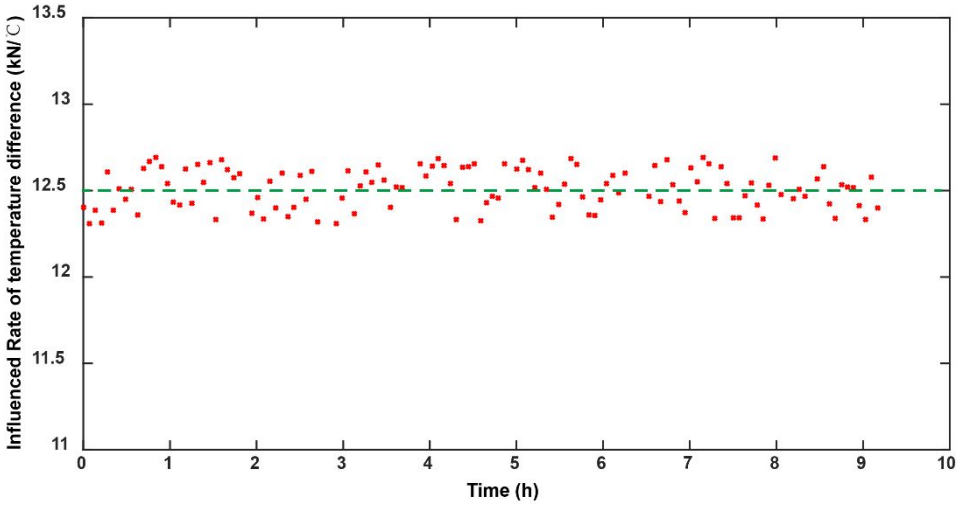

Fig.16—Influenced rate of temperature difference

It's clear that the experimental influenced rate fluctuated around 12.51, which is different from the simulated result 11.66 in Group 2. The reason is that the model used for simulating is simplified and the boundary conditions is also somewhat a little different from the real situation. During the experiment, the real WOB is zero. To validate the proposed new compensating method, the apparent WOB at the last moment is regarded as WOB_{a0}. The corrected WOB using Eq.18 is shown as **Fig.17**.

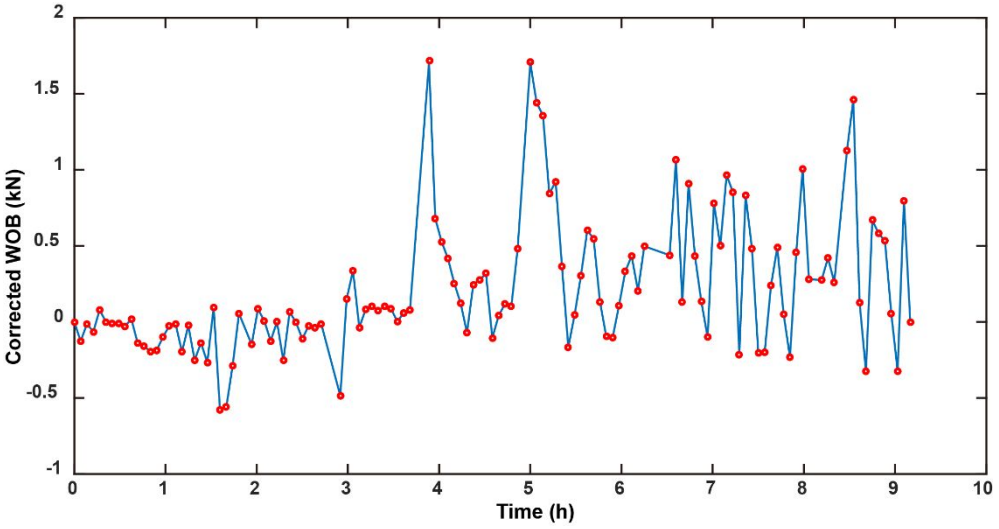

Fig.17—Corrected WOB

It can be concluded that the error can be largely eliminated using the new compensating method. The biggest error in Fig.17 is about 1.7kN, while the biggest error in Fig.15 is up to 60kN without considering the unstable thermal conduction stages.

4. Validation via the field experiment

To evaluate the influence of the non-uniform temperature distribution to the measurement of DWOB, a field experiment was conducted on a well located in Hebei, China. The experiment consisted of two stages: drilling cement and drilling formation. The Bottom Hole Assembly (BHA) below the measuring apparatus is shown in **Table. 3**.

Table. 3—BHA and its weight in different drilling conditions

	BHA below the measuring apparatus
Drilling	Φ215.9 mm cone bit ×0.24 m+430/410 adapter substitute×0.6 m+Φ177.8 mm

cement	nonmagnetic drill collar×9.15 m
Drilling formation	Φ215.9 mm PDC×0.32 m+Φ172 mm screw×8.15 m+Φ208 mm centralizer of screw×0.78 m+Φ177.8 mm nonmagnetic drill collar×9.15 m+Φ165 mm MWD×2.19 m

The pressure curves inside and outside the apparatus during the whole experiment are shown in **Fig.18**. The working conditions can be obtained from Fig.18.

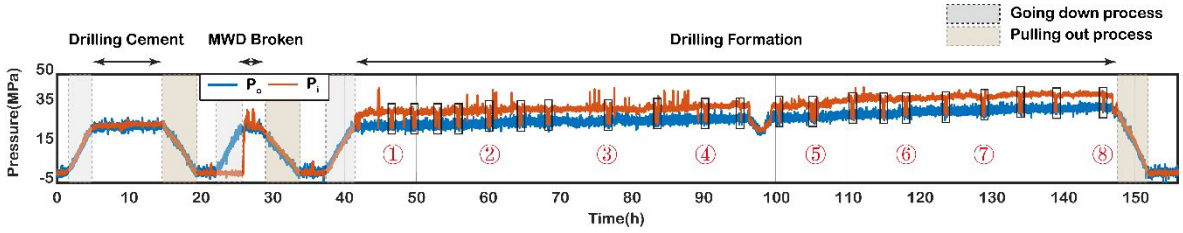

Fig.18—Inner pressure and outer pressure in the whole process

There is no doubt that the real DWOB is zero after turning off the pump, which can be used as the criterion to evaluate the new WOB correction method. When making a connection, it is necessary to turn off the pump. The connection processes are shown with black-framed rectangles in Fig.18.

The DWOB readings are closely correlated to the pressure inside and outside the measuring apparatus, the hydraulic friction, jet impingement force and temperature studied in the prior research works(Akimov et al., 2018; Wang et al., 2018; Winters and Warren, 1986a; Winters and Warren, 1986b). The hydraulic friction and jet impingement force are difficult to be calculated and measured precisely. Fortunately, their value in the process of connection turns to zero without drilling fluid circulating. And the pressure inside and outside the measuring apparatus stays steady, which is helpful to study the impact of the temperature difference to WOB readings separately.

The real DWOB in the hydrostatic environment without considering temperature difference can be expressed as(Wang et al., 2018)

$$WOB = T_c - \left(p_{out}A_o - p_{in}A_i\right) - \rho_l V g_i + \left(M_l + M_s\right) g_i \tag{19}$$

Here eight connection processes are chosen to elaborate the temperature difference impact and the related compensate method.

The raw WOB (WOBr) can be calculated using Eq.19, which is shown in **Fig.19** (a) and Fig.19 (b).

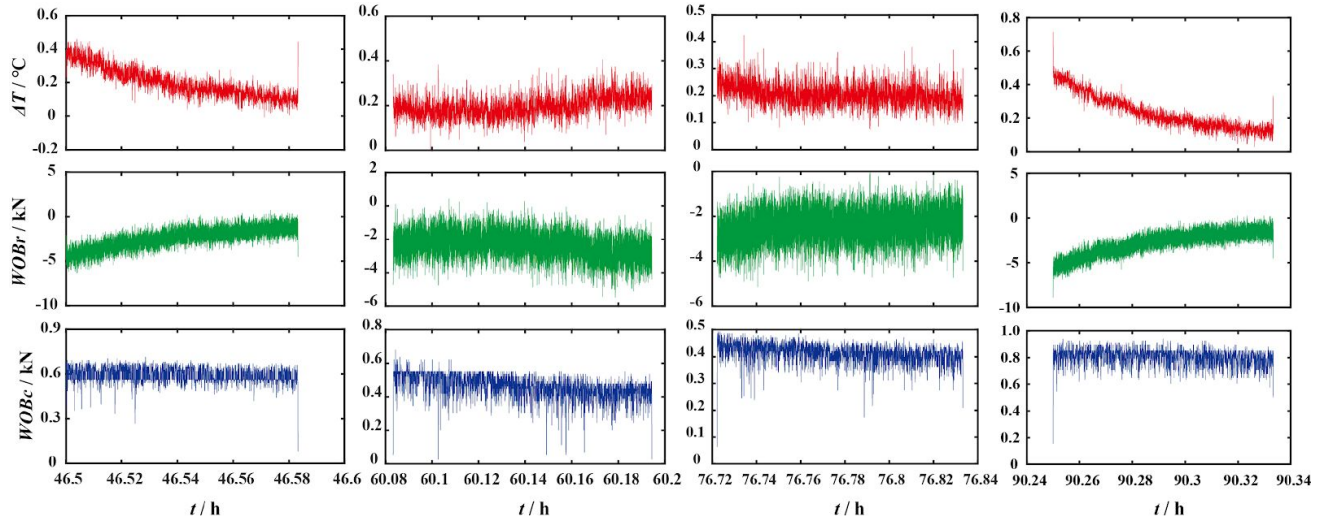

Fig.19 (a)—Temperature difference, raw WOB and corrected WOB curves of the first four stages

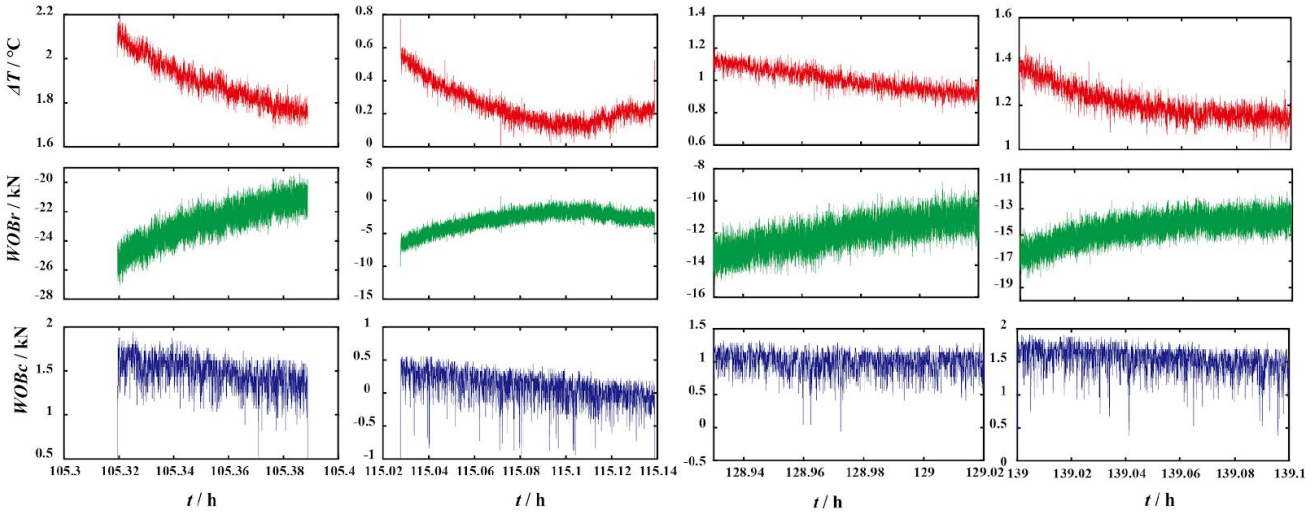

Fig.19 (b)—Temperature difference, raw WOB and corrected WOB curves of the second four stages

The WOBc in Fig.17 refers to the corrected WOB. When drilling, the heat of the measuring tool losses through the flowing fluid and gains from the radial heat conduction. And the two heat transferred ways are kept at a balanced point, leading to a temperature difference inside and outside the apparatus. After turning off the pump, the circulation of drilling fluid stops and there is no heat transferred along the well depth from downhole to the surface. Hence, the heat transfer is only the radial heat conduction. And the temperature difference turns to decrease, which has been shown in the three pictures of first row in Fig.19 (a) and Fig.19 (b).

The raw WOB (WOBr) increased when the temperature difference decreased, which coincided with the simulated results and the laboratory experiments. What's more, there is a strong negative correlation between Δt and WOBr seen from Fig.19. This indicated that temperature difference indeed affected the WOB readings.

A circulation process was chosen to be treated as the apparent WOB (WOB_{a0}) and the WOBc was determined depending on Eq.18. The corrected results indicated that the error had been eliminated to be around -0.5 kN ~ 3 kN. Much progress has been made using the proposed method to compensate the strain due to the non-uniform distribution of temperature.

5. Economic loss caused by the WOB measuring inaccuracy

According to the simulated results shown in Table.2 and the field experiment results shown in Fig.19, the apparent measured WOB is lower than the real WOB when taking no consideration of the non-uniform distribution of temperature in the measuring device. Namely, if the planned WOB is W_{opt}, the real WOB acted on the bit will be (W_{opt} +W_T). Where W_T is introduced by non-uniform distribution of temperature. Excessive WOB would cause the deduction of drill bit life and more trips, leading to more economic loss. Then the drilling cost per meter (C_{pm}) would increase accordingly. Here we use C_{pm} to evaluate the economic loss caused by the WOB measuring inaccuracy.

The calculation function of drilling cost per meter is

$$C_{pm}=\frac{C_r\left[\dfrac{t_e A_f\left(C_{n1}n+C_{n2}n^3\right)}{C_{W2}-C_{W1}W}+h_f+\dfrac{C_{th}}{2}h_f^2\right]}{C_pC_hC_{da}\left(W-W_{th}\right)n^{\lambda}\left[\dfrac{C_{th}}{C_{tv}}h_f+\dfrac{C_{tv}-C_{th}}{C_{tv}^2}\ln\left(1+C_{tv}h_f\right)\right]} \tag{20}$$

The expression of t_e is

$$t_e = \frac{C_b}{C_r} + t_{tr} + t_{cp} \tag{21}$$

Through calculating the partial derivatives from the target parameter C_{pm} to individual variables, we can get the optimal C_{pm}. The quantification of temperature difference's impact on WOB measurement is through the drilling cost loss percent per meter. The calculation parameters are shown in **Table. 4**.

Table. 4—Parameters for drilling cost per meter calculation

Parameters	Value	Parameters	Value
C_b	1200	C_{w2}	6.44
t_{tr}	5	h_f	1
t_{cp}	5	C_{th}	5
C_r	850	C_p	1
A_f	2.28×10^{-3}	C_h	1
C_{n1}	1.5	C_{da}	0.0023
C_{n2}	6.53×10^{-5}	W_{th}	10
n	67	λ	0.68
C_{w1}	0.0146	C_{ty}	3.68

Fig.20 shows the calculation results. When the temperature difference of the drilling tool's inside wall and the outside wall increases, the cost per drilling meter increases with a positive second derivative. The higher the rotating speed of the rotary table is, the less the cost is. According to the calculated stable temperature differences in Appendix A when the distance from the WOB measuring to the drill bit is 10 m, the related cost increase rate is about 0.04% using **Table. 5** simulating parameters and it is up to 1.17% using **Table. 6** simulating parameters.

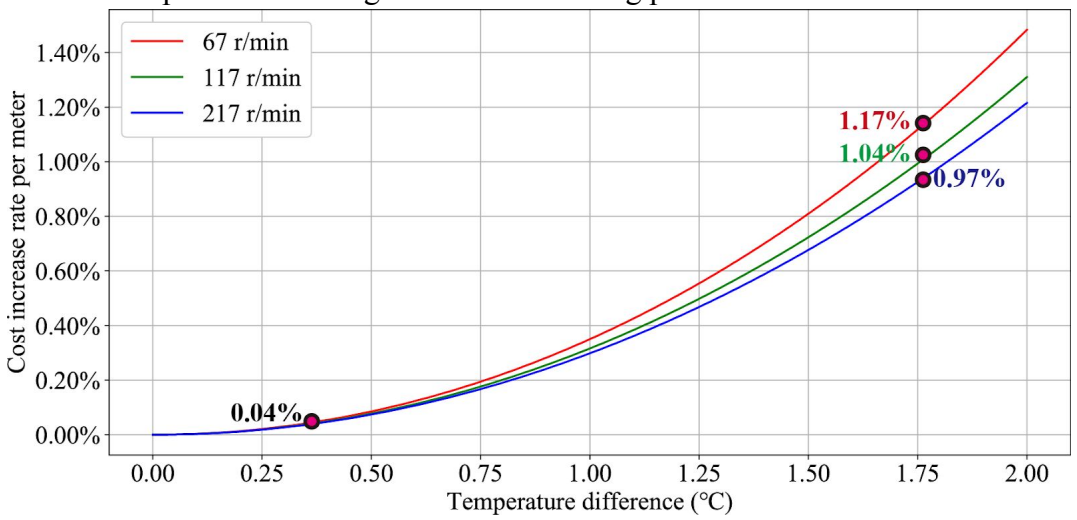

Fig.20—The drilling cost increasing rate with temperature difference

6. Conclusions

We herein calculated the temperature distributions of the WOB measuring device when the temperature difference between the inner wall and the outer wall is 0.8 ℃ and 4 ℃. To acquire the detailed strain of each measuring point when the temperature changed, we conducted three groups of simulation. The results showed that the thermal strain accounts for most of the total strain. Moreover, the circumferential strain due to temperature difference will increase to the same magnitude of the

circumferential strain due to outer force with the temperature difference increases. Wheatstone Bridges can ultimately eliminate the measuring error owing to thermal strain, but the influence of temperature difference between the inner wall and outer wall still could not be removed. The laboratory results have shown that the impact of the non-uniform distribution of temperature in the measuring device could not be neglected. Based on the transform of heat conduction equations, compatibility equations and constitutive equations, a novel compensatory method was established. Using this method to correct the simulated apparent WOB readings, the error was eliminated to 0.4 kN compared with the original error 46.25 kN. The laboratory experiment further validate the new method, with the original error 60 kN decreasing to 1.7 kN. A field experiment was conducted, which indicated that temperature difference indeed affected the WOB readings and the error had been eliminated to be around -0.5 kN ~ 3 kN using the new method.

When the real DWOB doesn't meet the designed optimal WOB, the time needed for drilling will increase and the life of the drilling bit will decrease, resulting in the low cost for drilling operations. The simulated drilling cost increase per meter in this paper is up to 1.17%.

7. Acknowledgments

The authors express their appreciation to the National Natural Science Foundation of China (Grant No.51734010, No.U1762211) and National Science and Technology Major Project (Grant No.2016ZX05020-003) for financial support to this paper.

8. Nomenclature

a	Thermal diffusivity, m^2/s
T	Temperature, ℃
q	Heat flu, J/m^2 s
κ	Thermal conductivity, W/m K
t	Time, s
T_{air}	Temperature of air inside the cavity, ℃
T_s	Temperature of steel , ℃
ε_i	i directional normal strain
γ_{ij}	Shear strain
$\boldsymbol{E}$	Strain tensor
E	Modulus of elasticity, Pa
μ	Poisson's ratio
$\boldsymbol{T}$	Stress tensor, Pa
Θ	The first principal invariants of the stress tensor, Pa
$T_{\text{innerWall}}$	Temperature of the inner wall, ℃
T_{inner}	Temperature of any inner point, ℃
$T_{\text{outerWall}}$	Temperature of the outer wall, ℃
K	gauge factor
α	Coefficient of thermal expansion, $(℃)^{-1}$
α_S	Coefficient of thermal expansion of substrate material, $(℃)^{-1}$
α_g	Coefficient of thermal expansion of the strain-gauge element, $(℃)^{-1}$
ΔT_{si}	The temperature change in the i^{th} strain gauge, , ℃

$\Delta\varepsilon_{\sigma i}$	The normal strain of the substrate where the i^{th} strain gauge is affixed
T_c	Axial force of the upper cross section, N
p_{out}	Annulus pressure while the drilling fluid is flowing, Pa
A_{o}	Area of the outer cross section, m^2
A_{i}	Area of the inner cross section, m^2
p_{in}	Inner pressure while the drilling fluid is flowing, Pa
$\rho_l V g_i$	i directional Buoyancy of the WOB measuring tool, N
$(M_l + M_s) g_i$	i directional gravity of the WOB measuring tool and the inside drilling fluid, N
C_{r}	The drilling rig operating expense per hour, ¥/h
A_{f}	The formation abrasiveness coefficient
C_{n1}, C_{n2}	Rotating speed influence coefficients
C_{th}	Tooth wear reduction factor
C_{w1}, C_{w2}	WOB influence coefficients
W	WOB, kN
h_{f}	The tooth wear loss
C_{p}	The fluid pressure difference influence coefficient
C_{h}	The hydraulic purification coefficient
C_{da}	The formation drill ability coefficient
W_{th}	WOB threshold, kN
λ	ROP index
C_{tv}	Tooth wear factor
C_{b}	The bit cost, ¥
t_{tr}	The trip time, h
t_{cp}	The taking single drill time, h

9. Appendix A. The quantification of temperature difference between the inside wall and the outside wall

Many studies have shown that the downhole temperature is the function of geothermal gradient, physical properties of drilling Fluids, surface pump rate and so on. Accordingly, the temperature difference of the annulus and the inside is also influenced by these factors. The temperature difference is not a fixed value, but varies with the formation conditions and drilling working conditions. To quantify the difference, we use the following calculated parameters, which is similar to the real drilling working conditions.

Table.5—Simulation parameters

Parameters	Value	Parameters	Value
Well depth	2600 m	Numbers of nozzle	3
Collar length	70 m	Temperature of pump drilling fluid	20 ℃
Upper casing length	2000 m	Surface temperature	20 ℃
Inside diameter of casing	244.5 mm	Geothermal gradient	0.03 ℃/m
Drill diameter	215.9 mm	Formation rock density	2600 kg/m^3
Outside diameter of drill strings	127 mm	Thermal conductivity of drilling fluid	1.73 W/(m·℃)
Inside diameter of drill strings	101 mm	Thermal conductivity of drill strings	43.75 W/(m·℃)
Outside diameter of collar	159 mm	Thermal conductivity of formation	2.25 W/(m·℃)

		rock	
Inside diameter of collar	73 mm	Specific heat of drilling fluid	3935 J/(kg·℃)
Nozzle diameter	26 mm	Specific heat of formation rock	837 J/(kg·℃)

We calculated the temperature distribution along the well depth with the typical wellbore temperature method(Jiang et al., 2019), which is shown in **Fig.21**. Considering that the WOB measuring tool is installed at a distance of 10 meters from the drill bit, we focused on this position's temperature difference.

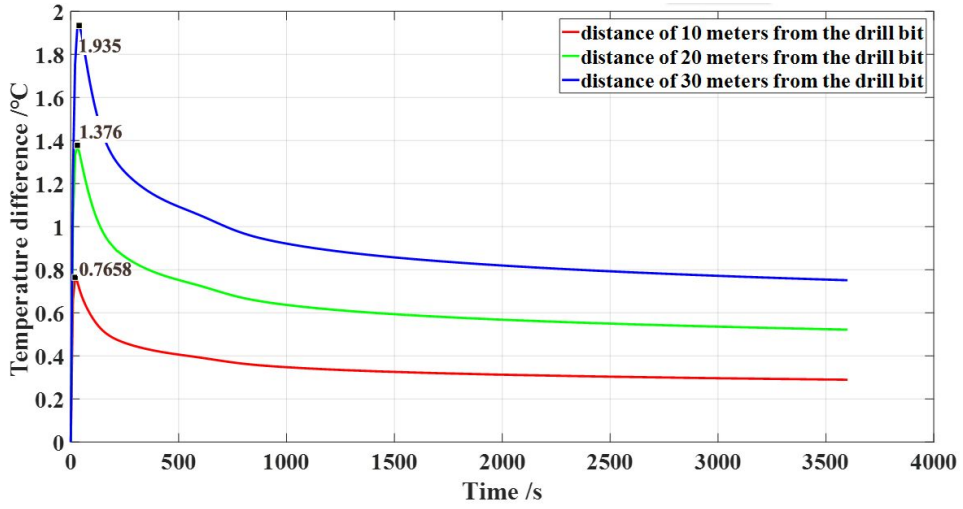

Fig.21—Temperature difference of the inside and the annulus in different positions

It's obvious that the temperature difference varies with the pumping time and position. After turning on the pump, the temperature difference increased to its peak value sharply and then decreased with a lower speed. What's more, the further the distance from the drill bit is, the larger the temperature difference is and the longer the time reaching the peak is. And this is the typical situation where drilling working conditions affect the temperature difference.

Here we calculated some factors' influence on the temperature difference at the distance of 10 meters from the drill bit. The result is shown in Fig.22.

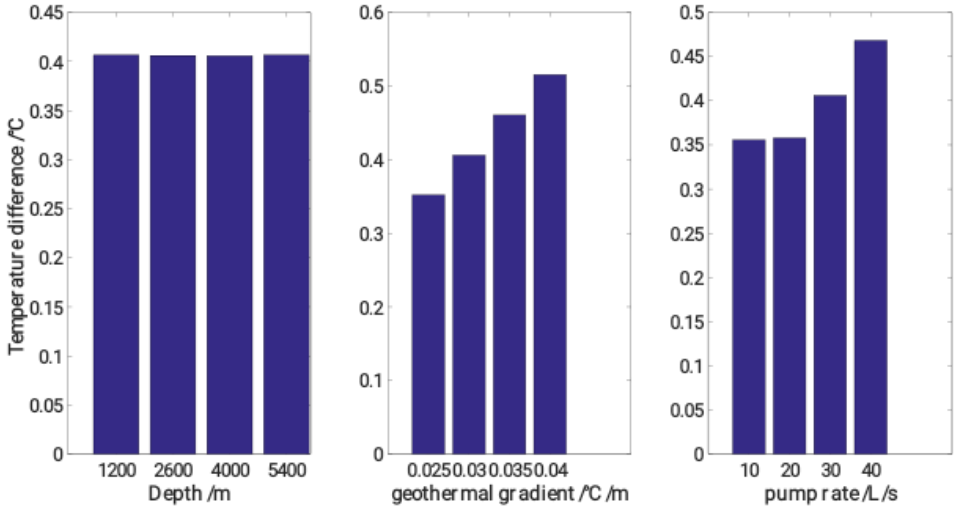

Fig.22—Temperature difference varying with depth, geothermal gradient and pump rate

It seems that the temperature difference has nothing to do with the drill bit's located depth when the rest parameters keep the same with **Table.5**. Temperature difference is sensitive to geothermal gradient, with the value varying from 0.35 ℃ to 0.51 ℃ when the geothermal gradient increased from 0.025 ℃/m to 0.04 ℃/m. This indicates that the formation parameters can influence the temperature difference. The pump rate can also affect the temperature difference and the relationship

is not linear, indicating the drilling fluid parameters can affect the temperature difference.

Next we calculate the temperature difference in another wellbore structure with different BHA and drilling fluid. The required parameters are shown in **Table.6**.

Table.6—Simulation parameters of another well

Parameters	Value	Parameters	Value
Well depth	5000 m	Numbers of nozzle	1
Collar length	200 m	Temperature of pump drilling fluid	20 ℃
Upper casing length	4000 m	Surface temperature	20 ℃
Inside diameter of casing	157 mm	Geothermal gradient	0.03 ℃/m
Drill diameter	157 mm	Formation rock density	2600 kg/m^3
Outside diameter of drill strings	88.9 mm	Thermal conductivity of drilling fluid	1.73 W/(m·℃)
Inside diameter of drill strings	70 mm	Thermal conductivity of drill strings	43.75 W/(m·℃)
Outside diameter of collar	88.9 mm	Thermal conductivity of formation rock	2.25 W/(m·℃)
Inside diameter of collar	70 mm	Specific heat of drilling fluid	1674 J/(kg·℃)
Nozzle diameter	16 mm	Specific heat of formation rock	837 J/(kg·℃)

The simulated result is shown in **Fig.23**.

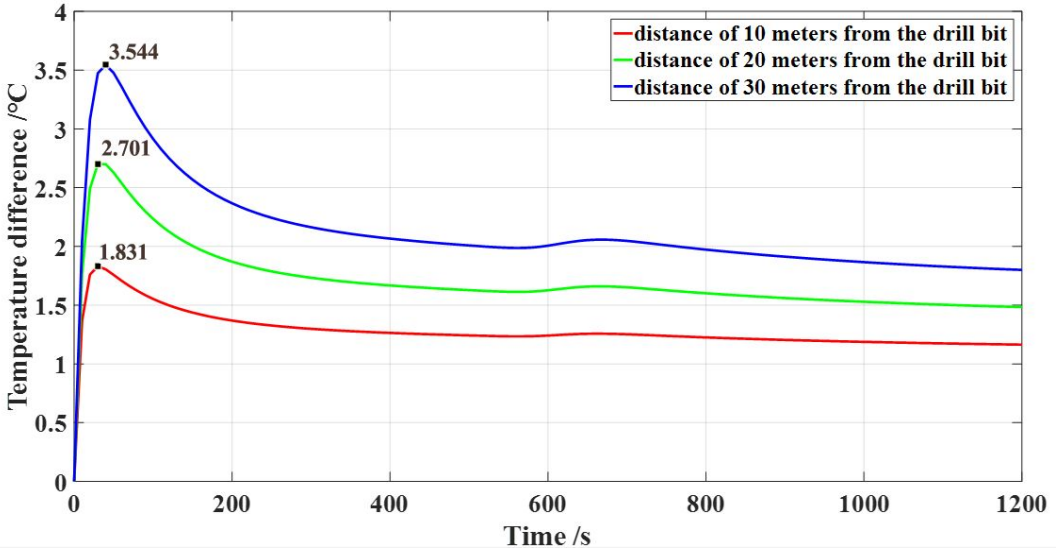

Fig.23—Temperature difference of the inside and the annulus in different positions of another well

In this well, the relative stable temperature difference is over 1 ℃. The trend of the temperature difference in Fig.23 varying with pump time is similar with that of Fig.21.

In summary, we can conclude that the temperature difference is not a fixed value and could not be calculated with an intuitive calculation formula.

10. Appendix B. The establishment of benchmark model

The heat transfer between the WOB measuring tool, the flowing fluid, and the formation influences the temperature difference of the inside wall and outside wall, leading to extra stress in the WOB measuring tool subsequently. The WOB measuring error comes into being at the same time. In fact, this is a thermo-solid coupling problem. The heat transfer relationship is shown in **Fig.24**.

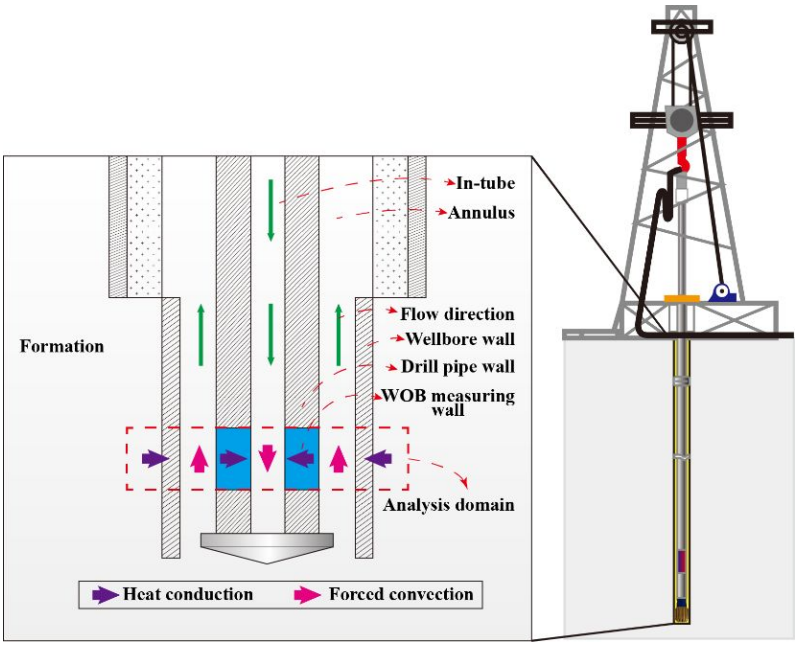

Fig.24—Schematic diagram of the heat transfer

Forced convection happens between the flowing drilling fluid and the WOB measuring tool. And heat conduction exists inside the measuring tool and the formation. To solve this thermo-solid coupling problem, the temperature distribution inside the WOB measuring tool should be obtained first and then inner thermal stress can be calculated.

Temperature of the inside wall, the outside wall, and the tool's two ends can be calculated using the wellbore temperature calculation method shown in Appendix.A. However, the temperature at the place where the strain gauges are pasted, cannot be acquired because of the large size of the simulation mesh. Hence, the measuring tool's mesh is refined and the fine temperature field can be calculated with the boundary conditions above. To simplify the simulation, we have made some assumption.

(1) The caps are considered as a part of the solid part and there is no need consideration of the contact relationship.

The caps are used to seal the measuring tool, preventing the inside circuits and microprocessors from the drilling fluid. This calls for no relative slip in tangential direction or relative separation in normal direction on the contact face of the caps and the groove. Hence, the contact type should be set to be "bonded" in simulation, which means the contact pair points share the same degree of freedom and this can be explained in **Fig.25**.

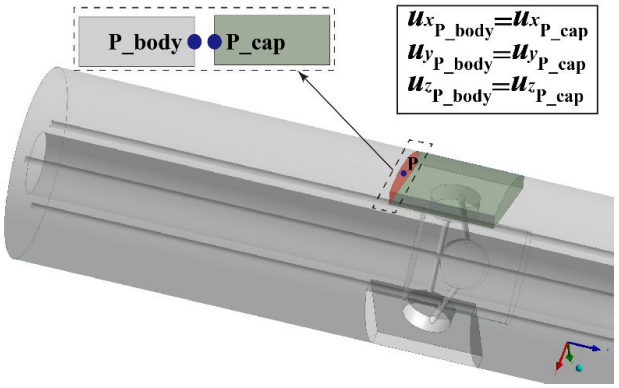

Fig.25—the "bounded" contact type. u_i is the *i* directional displacement

The norm strain ε_i and Shear strain γ_i of the contacting points will be the same deducing from Eq.4. According to the constitutive equation (Eq.22), the contact pair points' exerted force should

also be the same when the materials of the two contacted objects are the same.

$$\sigma_{ij} = \frac{E}{1+v}\varepsilon_{ij} + \frac{Ev}{(1+v)(1-2v)}\delta_{ij}e \tag{22}$$

This is to say, the caps and body can be treated as a whole when using "bounded" contact type. If the two parts are considered as a whole part, we need only one set of computing grids. Otherwise, we should make two sets computing grids and make sure that the grids in contact area should aligned.

(2) There is no consideration of the strain gauges modelling.

The strain gauges are used to measure the strain of the measured points. They are not allowed to change the original strain field to be measured.

The strain gauges are very thin which can help to prevent disturbing the original strain field. To prove this view point, we carried out three groups of simulations. The physical models and related results are shown in **Fig.26**.

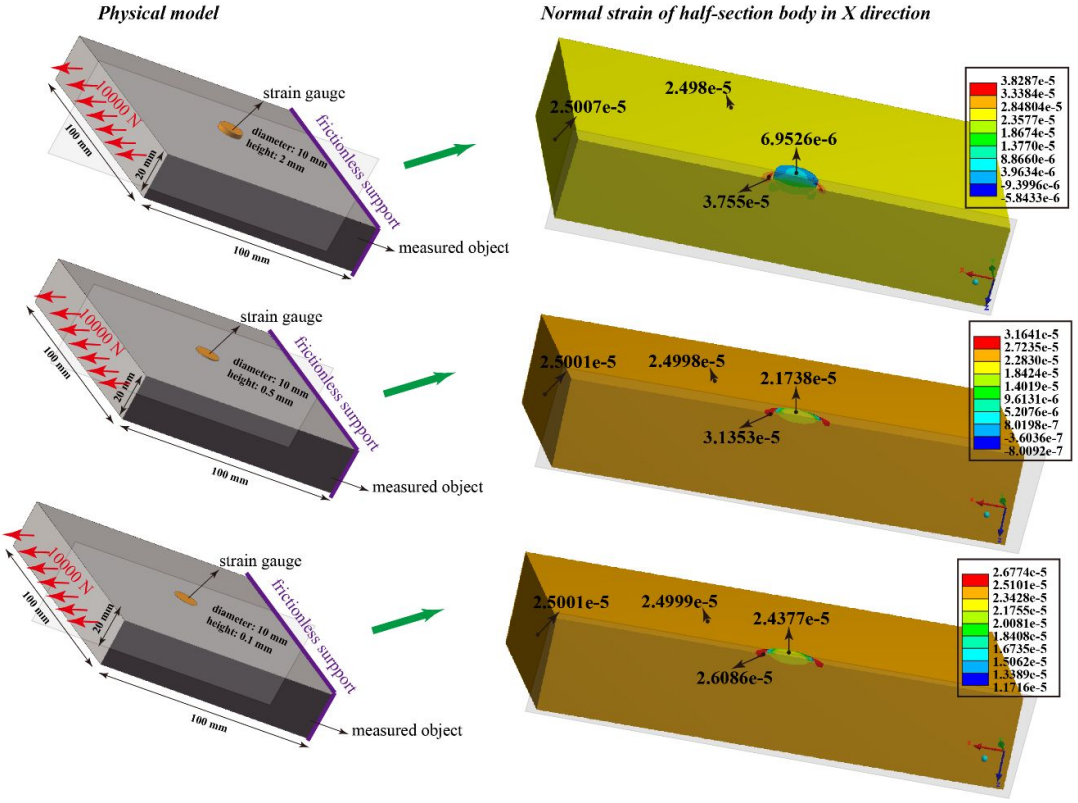

Fig.26—Influence of the strain gauge thickness to original field.

It is clear that the existence of pasted strain gauges will only change the strain field near the strain gauges seen in Fig.26. The more the distance from the strain gauges is, the less influence is. What's more, the smaller the thickness of the strain gauges, the less influence is. In the last simulation in Fig.26, the thickness is set to be 0.1 mm and the measured point's strain is not disturbed. However, the three kinds of strain gauge didn't change the measuring result. The reason is as follows.

When there is no force acting on the left side, the strain in the three group simulations is zero. Accordingly, we can calculate the gradient (k_i) of outer force to the measured strain. Then other outer force can be calculated with the following equation.

$$F - 10000N = k_i\left(\varepsilon_i - \varepsilon_{i0}\right) \tag{23}$$

Where ε_{i0} is the measured strain when the outer force is 1000 N and ε_i is the strain to be

measured when the outer force is *F*. Here *i* refers to the *ith* model in Fig.26.

To simplify the simulation model and guarantee the simulation process convergence, we choose to neglect the strain gauge when building the WOB measuring tool simulation model.

(3) The two ends of the simulated model are adiabatic

Using the parameters of Tab.1 in Appendix.A, we calculated the drill collar's end face temperature difference in 2580 m and 2590m. The result is shown in Fig.27.

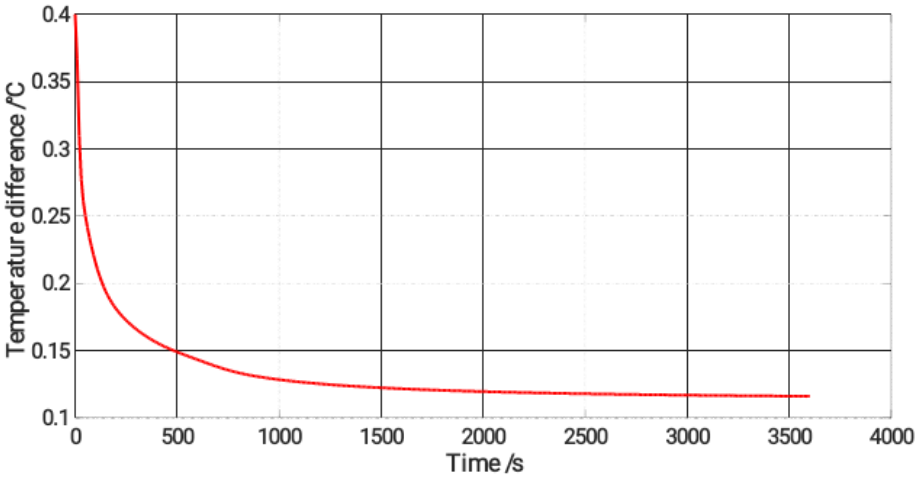

Fig.27—Drill collar's end face temperature difference in 2580 m and 2590 m

It can be found out that the temperature difference is around 0.12 ℃/10m axially from the calculated result in Fig.27. Radially, the temperature difference is around 69.77 ℃/10m calculated from Fig.21. Namely, the radial temperature difference is about 690 times of the axial temperature difference.

(4) Neglect the convective heat transfer in the cavity.

The cavity is used to hold the measuring circuits and the microprocessor and the rest room is filled with air. The thermal conductivity of air increases with temperature. When the environment temperature is 0 ℃ and 100 ℃, the thermal conductivity of air is 0.024 W/m·K and 0.031 W/m·K separately. Air is not conducive to heat conduction. The steel's thermal conductivity is 45 W/m·K. Steel is the component material of the WOB measuring tool. Namely, the steel's thermal conductivity is about 1451 times of the air's thermal conductivity.

With the above assumptions, the physical model and boundary conditions can be simplified as what **Fig.28** shows.

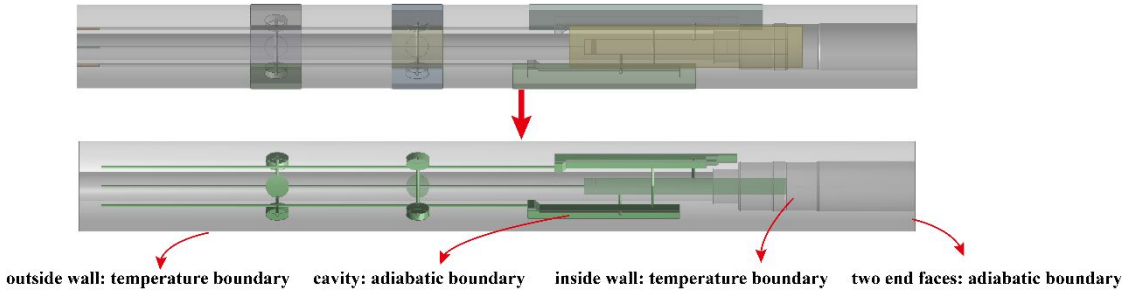

Fig.28— The simplified simulation model and boundary conditions

11. References

Akimov, O., Hohl, A., Oueslati, H. and Reckmann, H., 2018. Evolution of Drilling Dynamics Measurement Systems, SPE/IADC Middle East Drilling Technology Conference and Exhibition. Society of Petroleum Engineers, Abu Dhabi, UAE, pp. 13.

Al Saedi, A.Q., Flori, R.E. and Kabir, C.S., 2018. New analytical solutions of wellbore fluid temperature profiles during drilling, circulating, and cementing operations. Journal of Petroleum Science and Engineering, 170: 206-217.

Baumgartner, T., Ashok, P. and van Oort, E., 2019. Automated Preprocessing Techniques for High Frequency Downhole Sensor Data, SPE/IADC International Drilling Conference and Exhibition. Society of Petroleum Engineers, The Hague, The Netherlands, pp. 20.

Blanchette, C. and Getzlaf, D., 2015. New Downhole Data Clarifies Coiled Tubing Behavior in Horizontal Wells, SPE/CSUR Unconventional Resources Conference. Society of Petroleum Engineers, Calgary, Alberta, Canada.

Boucher, M.L., Schen, A., Ivie, C.R. and Jarvis, B.P., 2005. Apparatus for weight on bit measurements, and methods of using same. Google Patents.

Das, P.K. and Song, H., 1995. Load cells for sensing weight and torque on a drill bit while drilling a well bore. Google Patents.

Grosso, D.S., Raynal, J.C. and Rader, D., 1983. Report on MWD Experimental Downhole Sensors. SPE-2320-PA, 35(05): 899-904.

Hareland, G., Wu, A. and Lei, L., 2014. The Field Tests for Measurement of Downhole Weight on Bit(DWOB) and the Calibration of a Real-time DWOB Model, International Petroleum Technology Conference. International Petroleum Technology Conference, Doha, Qatar, pp. 6.

Holmes, C.S. and Swift, S.C., 1970. Calculation of Circulating Mud Temperatures. SPE-2320-PA, 22(06): 670-674.

Hutchinson, M., 2014. Apparatus and method for determining axial forces on a drill string during underground drilling. Google Patents.

Irawan, S., Mahfuz, A., Abd Rahman, A.M. and Tunio, S.Q., 2012. Optimization of Weight on Bit During Drilling Operation Based on Rate of Penetration Model. Research Journal of Applied Sciences, Engineering and Technology, 4.

Jia, B., Tsau, J.-S. and Barati, R., 2019. A review of the current progress of CO2 injection EOR and carbon storage in shale oil reservoirs. Fuel, 236: 404-427.

Jiang, H. et al., 2019. Model based fault diagnosis for drillstring washout using iterated unscented Kalman filter. Journal of Petroleum Science and Engineering, 180: 246-256.

Kabir, C.S., Hasan, A.R., Kouba, G.E. and Ameen, M., 1996. Determining Circulating Fluid Temperature in Drilling, Workover, and Well Control Operations. SPE-24581-PA, 11(02): 74-79.

Li, M., Liu, G., Li, J., Zhang, T. and He, M., 2015. Thermal performance analysis of drilling horizontal wells in high temperature formations. Applied Thermal Engineering, 78: 217-227.

Mason, C. and Chen, D.C.K., 2007. Step Changes needed to Modernise T&D Software, SPE/IADC Drilling Conference. Society of Petroleum Engineers, Amsterdam, The Netherlands, pp. 12.

Pink, A.P., Kverneland, H., Bruce, A. and Applewhite, J.B., 2012. Building an Automated Drilling System Where the Surface Machines are Controlled by Downhole and Surface Data to Optimize the Well Construction Process, IADC/SPE Drilling Conference and Exhibition. Society of Petroleum Engineers, San Diego, California, USA, pp. 9.

Pink, T.P., Koederitz, W.L., Barrie, A., Bert, D.R. and Overgaard, D.C., 2013. Closed Loop Automation Of Downhole Weight On Bit Improves Sliding Performance And Reduces Conservatism In Unconventional Horizontal Well Development, SPE Annual Technical Conference and Exhibition. Society of Petroleum Engineers, New Orleans, Louisiana, USA, pp. 14.

Ramey, H.J., Jr., 1962. Wellbore Heat Transmission. SPE-2320-PA, 14(04): 427-435.

Roberts, T.S., Schen, A.E. and Wise, J.L., 2005. Optimization of PDC Drill Bit Performance Utilizing High-Speed, Real-Time Downhole Data Acquired Under a Cooperative Research and Development Agreement, SPE/IADC Drilling Conference. Society of Petroleum Engineers, Amsterdam, Netherlands, pp. 14.

Saeid, S., Al-Khoury, R. and Barends, F., 2013. An efficient computational model for deep low-enthalpy geothermal systems. Computers & Geosciences, 51: 400-409.

Saputelli, L., Economides, M., Nikolaou, M. and Kelessidis, V., 2003. Real-Time Decision-making for Value Creation while Drilling, SPE/IADC Middle East Drilling Technology Conference and Exhibition. Society of Petroleum Engineers, Abu Dhabi, United Arab Emirates, pp. 19.

Shi, Y. et al., 2018. Numerical investigation on heat extraction performance of a CO2 enhanced geothermal system with multilateral wells. Energy, 163: 38-51.

Shi, Y. et al., 2019a. Numerical study on heat extraction performance of a multilateral-well enhanced geothermal system considering complex hydraulic and natural fractures. Renewable Energy, 141: 950-963.

Shi, Y. et al., 2019b. Study on wellbore fluid flow and heat transfer of a multilateral-well CO2 enhanced geothermal system. Applied Energy, 249: 14-27.

Song, X. et al., 2017. Heat extraction performance simulation for various configurations of a downhole heat exchanger geothermal system. Energy, 141: 1489-1503.

Sutcliffe, B. and Sim, D., 1991. Drilling optimized by monitoring BHA dynamics with MWD. Oil and Gas Journal, 89:12.

Taler, J. et al., 2018. Monitoring of thermal stresses in pressure components based on the wall temperature measurement. Energy, 160: 500-519.
Taler, J., Zima, W. and Jaremkiewicz, M., 2016. Simple method for monitoring transient thermal stresses in pipelines. Journal of Thermal Stresses, 39(4): 386-397.
Tanguy, D.R. and Leising, L.J., 1982. Weight-on-bit and torque measuring apparatus. Google Patents.
Wachtler, W.J. and Yang, T.M., 1986. MWD tool for measuring weight and torque on bit. Google Patents.
Wang, C. et al., 2018. New methods of eliminating downhole WOB measurement error owing to temperature variation and well pressure differential. Journal of Petroleum Science and Engineering, 171: 1420-1432.
Wassell, M.E., 2003. Apparatus for measuring weight and torque on drill bit operating in a well. Google Patents.
Wassell, M.E., Cobern, M.E. and Perry, C.A., 2013. Apparatus for measuring bending on a drill bit operating in a well. Google Patents.
Winters, W.J. and Warren, T.M., 1986a. Field Application of Diamond-bit Hydraulic-Lift Principles (includes associated papers 17470 and 17553).
Winters, W.J. and Warren, T.M., 1986b. Laboratory Study of Diamond-Bit Hydraulic Lift (includes associated papers 17470 and 17553).
Woloson, S.E. and Jones, D.A., 2001. Apparatus for measuring downhole drilling efficiency parameters. Google Patents.
Wu, A. and Hareland, G., 2012. Calculation of Friction Coefficient And Downhole Weight On Bit With Finite Element Analysis of Drillstring, 46th U.S. Rock Mechanics/Geomechanics Symposium. American Rock Mechanics Association, Chicago, Illinois, pp. 6.
Xu, C., Dowd, P.A. and Tian, Z.F., 2015. A simplified coupled hydro-thermal model for enhanced geothermal systems. Applied Energy, 140: 135-145.
Yao, J. et al., 2018. Numerical simulation of the heat extraction in 3D-EGS with thermal-hydraulic-mechanical coupling method based on discrete fractures model. Geothermics, 74: 19-34.
Zha, Y., Ramsay, S. and Pham, S., 2018. Real Time Surface Data Driven WOB Estimation and Control, SPE Annual Technical Conference and Exhibition. Society of Petroleum Engineers, Dallas, Texas, USA, pp. 17.
Zhang, S. et al., 2018. Numerical analysis of transient conjugate heat transfer and thermal stress distribution in geothermal drilling with high-pressure liquid nitrogen jet. Applied Thermal Engineering, 129: 1348-1357.